Keap1 loss promotes *Kras*-driven lung cancer and results in dependence on glutaminolysis

Rodrigo Romero[1,2,15], Volkan I Sayin[3,15], Shawn M Davidson[1,2], Matthew R Bauer[1], Simranjit X Singh[3], Sarah E LeBoeuf[3], Triantafyllia R Karakousi[3], Donald C Ellis[1,2], Arjun Bhutkar[1], Francisco J Sánchez-Rivera[1,2], Lakshmipriya Subbaraj[1,2], Britney Martinez[3], Roderick T Bronson[4,5], Justin R Prigge[6], Edward E Schmidt[6], Craig J Thomas[7], Chandra Goparaju[8], Angela Davies[9], Igor Dolgalev[10], Adriana Heguy[10], Viola Allaj[11,12], John T Poirier[11,12], Andre L Moreira[3], Charles M Rudin[11,12], Harvey I Pass[8], Matthew G Vander Heiden[1,2], Tyler Jacks[1,2,13] & Thales Papagiannakopoulos[3,14]

Treating **KRAS**-mutant lung adenocarcinoma (LUAD) remains a major challenge in cancer treatment given the difficulties associated with directly inhibiting the KRAS oncoprotein[1]. One approach to addressing this challenge is to define mutations that frequently co-occur with those in **KRAS**, which themselves may lead to therapeutic vulnerabilities in tumors. Approximately 20% of **KRAS**-mutant LUAD tumors carry loss-of-function mutations in the **KEAP1** gene encoding Kelch-like ECH-associated protein 1 (refs. 2–4), a negative regulator of nuclear factor erythroid 2-like 2 (**NFE2L2**; hereafter **NRF2**), which is the master transcriptional regulator of the endogenous antioxidant response[5–10]. The high frequency of mutations in **KEAP1** suggests an important role for the oxidative stress response in lung tumorigenesis. Using a CRISPR–Cas9-based approach in a mouse model of KRAS-driven LUAD, we examined the effects of *Keap1* loss in lung cancer progression. We show that loss of *Keap1* hyperactivates NRF2 and promotes KRAS-driven LUAD in mice. Through a combination of CRISPR–Cas9-based genetic screening and metabolomic analyses, we show that *Keap1*- or *Nrf2*-mutant cancers are dependent on increased glutaminolysis, and this property can be therapeutically exploited through the pharmacological inhibition of glutaminase. Finally, we provide a rationale for stratification of human patients with lung cancer harboring **KRAS**/**KEAP1**- or **KRAS**/**NRF2**-mutant lung tumors as likely to respond to glutaminase inhibition.

Genetically engineered mouse models (GEMMs) of lung cancer have greatly assisted in the functional characterization of genes implicated in human lung cancers. The *loxP*-STOP-*loxP* (LSL)-*Kras*^G12D/+; *Tp53*^flox/flox (*p53*) (KP) GEMM of human LUAD faithfully mimics human KRAS-driven LUAD, displaying similarities at the molecular and histopathological levels following intratracheal administration of viral vectors expressing Cre recombinase[11]. We recently developed a CRISPR–Cas9-based *in vivo* genome-engineering method to rapidly interrogate putative genetic driver events cooperating with oncogenic *Kras* to promote lung tumorigenesis in the KP model[12–14].

On the basis of the fact that *KEAP1* is the third most frequently mutated gene in human LUAD and the high coincidence of inactivating mutations in *KEAP1* with *KRAS* mutation in human lung cancers[3], we chose to target *Keap1* in the KP model using CRISPR–Cas9 technology. KP mice were intratracheally infected with pSECC lentiviral vectors expressing single-guide RNAs (sgRNAs) against *Keap1* or *tdTomato* as a control (hereafter referred to as sg*Keap1* and sg*Tom* mice, respectively; **Supplementary Fig. 1a**). sg*Keap1* mice had a significantly increased tumor burden and faster tumor growth kinetics when compared to sg*Tom* mice, as determined by longitudinal micro-computed tomography (micro-CT; $P < 0.05$; **Fig. 1a**). In accordance with the micro-CT data, histological assessment revealed a significant increase in tumor burden in sg*Keap1* mice as compared to controls ($P < 0.05$; **Fig. 1b**). This analysis also showed a dramatic increase in the number of aggressive high-grade tumors in sg*Keap1* mice as compared to controls ($P < 0.0001$ for sg*Keap1.2* grade 3 tumors and $P < 0.001$ for sg*Keap1.4* grade 4 tumors; **Fig. 1c** and **Supplementary Fig. 1b**). Furthermore, tumors in sg*Keap1* mice displayed increased proliferation as gauged by an increase in mitotic index (marked by phosphorylated histone H3; $P < 0.05$; **Fig. 1d**).

[1]Koch Institute for Integrative Cancer Research, Massachusetts Institute of Technology, Cambridge, Massachusetts, USA. [2]Department of Biology, Massachusetts Institute of Technology, Cambridge, Massachusetts, USA. [3]Department of Pathology, New York University School of Medicine, New York, New York, USA. [4]Tufts University, Boston, Massachusetts, USA. [5]Harvard Medical School, Boston, Massachusetts, USA. [6]Department of Immunology and Infectious Diseases, Montana State University, Bozeman, Montana, USA. [7]National Institutes of Health Chemical Genomics Center, Division of Preclinical Innovation, National Center for Advancing Translational Sciences, US National Institutes of Health, Bethesda, Maryland, USA. [8]Department of Cardiothoracic Surgery, New York University Langone Medical Center, New York, New York, USA. [9]Champions Oncology, Hackensack, New Jersey, USA. [10]Genome Technology Center, New York University School of Medicine, New York, New York, USA. [11]Molecular Pharmacology Program, Memorial Sloan Kettering Cancer Center, New York, New York, USA. [12]Department of Medicine, Memorial Sloan Kettering Cancer Center, New York, New York, USA. [13]Howard Hughes Medical Institute, Chevy Chase, Maryland, USA. [14]Perlmutter Cancer Center, New York University School of Medicine, New York, New York, USA. [15]These authors contributed equally to this work. Correspondence should be addressed to T.J. (tjacks@mit.edu) or T.P. (papagt01@nyumc.org).
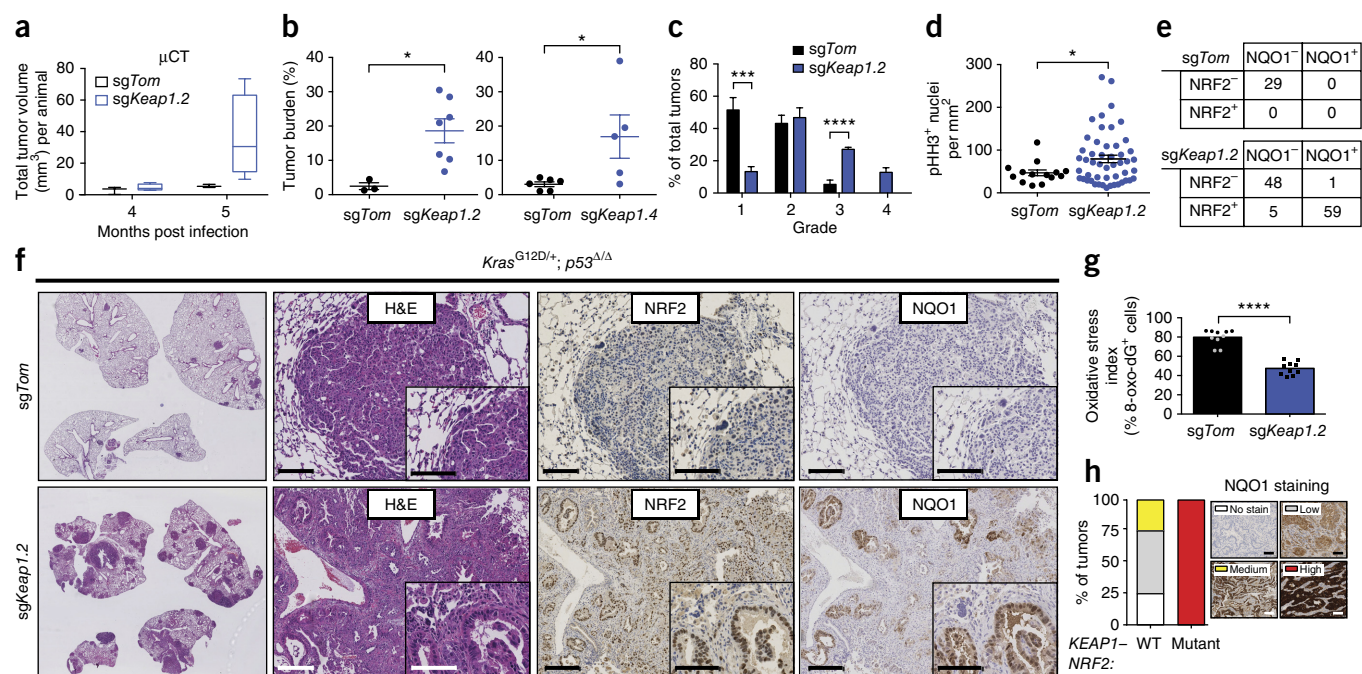
Figure 1 Loss of *Keap1* stabilizes NRF2 and accelerates lung tumorigenesis. (**a**) Micro-CT quantification of total tumor volume (mm³) for tumors from sg*Keap1.4* or sg*Tom* mice (*n* = 5 and 3, respectively) at 4 and 5 months after infection. Whiskers represent minimum and maximum values, upper and lower perimeters represent the interquartile distance, and midlines represent mean values. (**b**) Combined quantification of tumor burden (total tumor area/total lung area) in KP mice after infection with pSECC lentiviruses. Left, tumor burden of mice infected with control sg*Tom* (*n* = 3) or sg*Keap1.2* (*n* = 7) at 21 weeks after infection. Right, tumor burden in mice infected with control sg*Tom* (*n* = 6) or sg*Keap1.4* (*n* = 5) at 21 weeks after infection. Asterisks indicate statistical significance obtained from comparing KP-sg*Keap1* samples to KP-sg*Tom* samples. (**c**) Distribution of histological tumor grades in KP mice 21 weeks after infection with pSECC lentiviruses expressing control (sg*Tom* KP, *n* = 7 mice) or *sgKeap1.2* (KP; *n* = 3 mice). (**d**) Quantification of phosphorylated histone H3 (pHH3)-positive nuclei per squared millimeter of tumor for assessment of the mitotic index of tumor cells from lung tumors in KP mice at 21 weeks after infection with pSECC lentiviruses expressing control (sg*Tom*; *n* = 14 tumors) or sg*Keap1.2* (*n* = 50 tumors). (**e**) Contingency tables demonstrating the correlation between nuclear NRF2 expression and NQO1 expression. Top, quantified tumors obtained from control sg*Tom* mice. Bottom, quantified tumors obtained from sg*Keap1.2* mice. (**f**) Representative H&E and IHC staining of serial sections from lung tumors of mice 21 weeks after infection with pSECC-sg*Tom* (top) or pSECC-sg*Keap1.2* (bottom). First panels, overall lung tumor burden; second panels, higher-magnification H&E staining of representative tumors; third panels, nuclear NRF2 IHC analyses; fourth panels, NQO1 IHC analyses. Note that the accumulation of NRF2 and NQO1 occurs only in tumors from pSECC-*sgKeap1.2* mice. Insets show higher-magnification images. Images are representative of 29 and 113 tumors from sg*Tom*-infected (*n* = 3) and sg*Keap1.2*-infected (*n* = 7) mice, respectively. Scale bars, 100 µm. (**g**) Oxidative stress index as assessed by the percentage of 8-oxo-2′-deoxyguanosine (8-oxo-dG)-positive nuclei (*n* = 10 per genotype). (**h**) IHC analyses for NQO1 of *KEAP1*- or *NRF2*-mutant human LUAD biopsies versus biopsies WT for both genes. All tumor samples were confirmed to be *KEAP1*- or *NRF2* mutant via targeted exome sequencing (**Supplementary Table 1**). Right, examples of staining criteria. Data are presented as means, with error bars denoting s.e.m. Statistical analyses in **b**–**d** and **g** were performed using two-sided Student's *t*-tests and in **e** were performed with two-sided Fisher's exact tests. *P < 0.05, ***P < 0.001, ****P < 0.0001.

To determine the activation status of the KEAP1–NRF2 pathway in tumors from sg*Keap1* mice, we performed immunohistochemical (IHC) analyses to assess whether loss of *Keap1* led to both increased nuclear localization of NRF2 protein and higher cytoplasmic levels of the protein encoded by its target *Nqo1* (NAD(P)H dehydrogenase quinone 1). The majority of tumors (60%) in sg*Keap1* mice had increased nuclear localization of NRF2 and dramatically higher levels of NQO1 as compared to controls (*P* < 0.0001; **Fig. 1e,f**). Notably, nearly all tumors that stained positively for nuclear NRF2 also contained higher levels of NQO1 (*P* < 0.0001; **Fig. 1e**). Furthermore, the increased levels of nuclear NRF2 in tumors from sg*Keap1* mice correlated with significantly lower reactive oxygen species (ROS)-dependent oxidation of DNA as compared to tumors in control sg*Tom* mice (**Fig. 1g**). High-throughput DNA sequencing of microdissected tumors from sg*Keap1* mice (sg*Keap1.2* and sg*Keap1.4*) that stained positively for NQO1 and nuclear NRF2 revealed that these tumors predominantly harbored frameshift loss-of-function (LOF) insertions or deletions (indels) in *Keap1*, supporting the results of the IHC analysis indicating

NRF2 pathway activation (**Supplementary Fig. 1c–e**). Additionally, we observed clonal enrichment of these *Keap1* LOF alleles in a lymph node metastasis in comparison to the paired primary tumor[15,16] (**Supplementary Fig. 1f–h**).

We next asked whether NQO1 could act as a marker for *KEAP1*–*NRF2*-mutant human LUAD tumors with NRF2 activation. Targeted exome capture (for the 50 most frequently mutated genes in LUAD, based on The Cancer Genome Atlas (TCGA)[3] data) of 88 LUAD tumors from the New York University Center for Biospecimen Research and Development identified 10 *KEAP1*- and 2 *NRF2*-mutant tumors (11% and 2%, respectively), as well as a significant correlation between either *KEAP1* or *NRF2* mutations and increased NQO1 staining (*P* = 0.0002; **Fig. 1h** and **Supplementary Table 1**). These data suggest that NQO1 is a suitable biomarker for NRF2 activation in human LUAD.

To determine the role of NRF2 and KEAP1 in the regulation of proliferation and antioxidant pathways in LUAD, we used CRISPR–Cas9-mediated genome editing to develop isogenic KP-derived lung tumor cell lines with LOF mutations in *Nrf2* (KPN) or *Keap1* (KPK), and

sgTom controls (KP) ($n = 2$ cell lines per genotype; **Supplementary Fig. 2a,b**). As expected, KPK cells had increased nuclear localization of NRF2 and increased levels of NRF2 transcriptional targets as assessed by both protein analysis (using glutamate–cysteine ligase catalytic subunit (GCLC); **Supplementary Fig. 2c**) and gene expression analysis (using *Nqo1*, *Hmox1*, and *Gclc*; **Supplementary Fig. 2d**). These changes were also observed in KP but not KPN cells upon treatment with NRF2 activators (**Supplementary Fig. 2e–h**). To validate these results, we performed whole-transcriptome analyses (RNA-seq) and identified transcriptional signatures that clearly distinguished KP from KPK cell lines on the basis of activation of the NRF2 transcriptional program (**Supplementary Fig. 2i** and **Supplementary Table 2**).

We next used this panel of genetically defined cell lines to further explore the role of the NRF2–KEAP1 pathway in regulating the antioxidant response program. KPN cells had dramatically decreased cell viability as compared to KP cells in response to multiple agents known to cause oxidative stress. In contrast, KPK cells showed resistance to all agents tested (**Supplementary Fig. 3a–e**). These effects correlated with total levels of the major cellular antioxidant glutathione in the different cell lines (**Supplementary Fig. 3f,g**). The loss of viability of KPN cells in response to oxidative-stress-inducing agents was rescued by antioxidant treatments (**Supplementary Fig. 3h**) or by ectopic expression of an *Nrf2* allele with a gain-of-function (GOF) mutation (*Nrf2*-GOF)[17] (cells transduced with *Nrf2*-GOF cDNA were denoted KPN-ix cells; **Supplementary Fig. 3i–o**). In accordance with these results, *Keap1*- and *KEAP1*-mutant cells in mouse and human both displayed markedly lower ROS levels than wild-type (WT) cells (**Supplementary Fig. 3p,q**). Interestingly, KPK cells grew faster than KP cells *in vivo* but not *in vitro* (**Supplementary Fig. 4a–f**), suggesting a differential requirement for the NRF2–antioxidant pathway during tumorigenesis *in vivo*. In addition, loss of *Keap1* or *KEAP1* in tumors and cells with wild-type *p53* (ref. 18) accelerated tumorigenesis and growth, suggesting that *Keap1* is a tumor suppressor in lung cancer progression that acts independently of *p53* mutation status (**Supplementary Fig. 5a–p**). These data indicate that NRF2 levels dictate the differential antioxidant response to oxidative stress, which may provide a selective growth advantage *in vivo*.

To assess the relevance of these data derived from GEMM studies to human lung cancer, we performed an integrative analysis using a data set of human LUAD samples ($n = 548$) from TCGA[3], published NRF2 data sets[7,19,20], and our GEMM-derived NRF2-driven transcriptional signature. First, we derived a core NRF2 signature from 108 high-confidence NRF2 target genes (**Supplementary Table 3**) using published data sets. TCGA human LUAD tumors across various disease stages were investigated; core NRF2 target genes were significantly upregulated in tumors from advanced-stage (stage 4) disease ($P = 0.028$; **Fig. 2a**). Additionally, subjects whose tumors were most associated with the NRF2 core signature had significantly worse survival than the rest of the TCGA LUAD cohort ($P = 0.008$; **Fig. 2b**). In order to evaluate the association between *KEAP1* mutations and NRF2 pathway activation, we used gene expression data from all TCGA human LUAD primary tumors to derive a transcriptional signature for *KEAP1*-mutant tumors (**Supplementary Fig. 6a**). This signature was enriched in core NRF2 target genes, multiple antioxidant pathways, and the NRF2 oncogenic signature[19] (NFE2L2.V2; **Supplementary Fig. 6b,c** and **Supplementary Table 4**). Ranking tumors by the strength of their correlation with this signature allowed for stratification of all TCGA subjects with LUAD into two subpopulations ($n = 91$ corresponding to the 20% with the highest
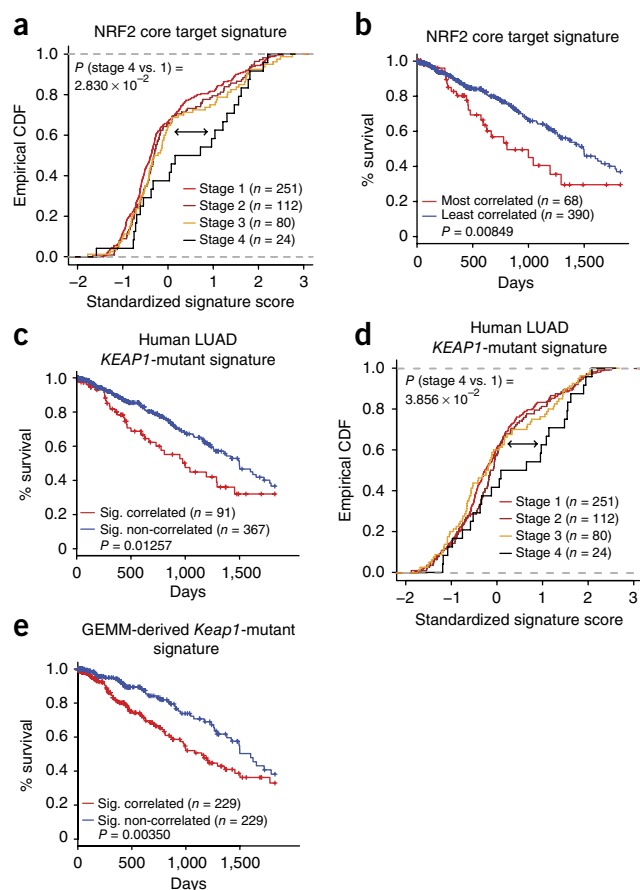

Figure 2 An NRF2 target gene signature and a human-derived *KEAP1*-mutant signature predict survival of human subjects with LUAD. (**a**) Empirical cumulative distribution function (CDF) plots showing correlation of individual tumors with the NRF2 core target signature across various clinical stages within the TCGA LUAD cohort. Each curve in the plot represents a unique clinical stage. Clinical stage 4 tumors ($n = 24$) are highly correlated with the NRF2 core target signature and are significantly different as compared to lower-stage (stage 1) tumors ($n = 251$; $P = 0.028$, Kolmogorov–Smirnov test). (**b**) Kaplan–Meier (KM) survival curves comparing subjects in the TCGA LUAD cohort stratified by correlation with the NRF2 core target signature. Tumor samples were binned according to their gene expression correlation with the NRF2 signature. Subjects harboring the top 15% ($n = 68$) most correlated tumors exhibited significantly decreased survival as compared to the remaining subjects ($n = 390$) from the TCGA LUAD cohort ($P = 0.008$, log-rank test). (**c**) KM survival curves comparing subjects in the TCGA LUAD cohort stratified by correlation with the *KEAP1*-mutant signature derived from TCGA expression profiles of the subjects. The top 20% most correlated subjects ($n = 91$) exhibited decreased survival as compared to the remaining subjects ($n = 367$) from the TCGA LUAD cohort ($P = 0.012$, log-rank test). Sig., significantly. (**d**) CDF plots showing expression correlation of individual tumors with the *KEAP1*-mutant signature across various clinical stages within the TCGA LUAD cohort. Each curve represents a unique clinical stage. Clinical stage 4 tumors ($n = 24$) are highly correlated with the *KEAP1*-mutant signature and are significantly different from stage 1 tumors ($n = 251$; $P = 0.038$, Kolmogorov–Smirnov test). Gray dashed lines in **a** and **d** indicate minimum and maximum values. (**e**) KM survival curves comparing subjects in the TCGA LUAD cohort stratified by correlation with the mouse-derived *Keap1*-mutant signature. The top 50% most correlated tumors ($n = 229$) exhibited significantly decreased survival as compared to the remaining tumors ($n = 229$) from the TCGA LUAD cohort ($P < 0.003$, log-rank test).

correlation and $n = 367$ corresponding to the remainder of the cohort). These subpopulations exhibited significantly different survival times

($P = 0.012$; **Fig. 2c**). Similar results were observed within the set of subjects harboring mutated *KRAS* ($n = 24$ corresponding to the 20% with the highest correlation and $n = 99$ corresponding to the remainder of the cohort; $P = 0.00013$; **Supplementary Fig. 6d**). We did not observe significant co-occurrence of *KEAP1*-mutant and *KRAS*-mutant subjects within the TCGA cohort ($P = 0.418$). Additionally, among the top 20% of subjects whose tumors showed correlation with our *KEAP1*-mutant signature and who exhibited poor survival, we did not observe enrichment for *KRAS*-mutant subjects ($P = 0.816$) when compared to the background prevalence of *KRAS*-mutant individuals in the TCGA cohort. Taken together, these data suggest that the poor survival of the subjects whose tumors had the highest correlation with the *KEAP1*-mutant signature cannot be attributed to an over-representation of *KRAS*-mutant subjects.

Furthermore, high-grade tumors (grade 3 or 4) and late-stage tumors (clinical stage 4 disease) were significantly enriched for the human *KEAP1*-mutant transcriptional signature (grade 3 or 4, $P = 0.02$; clinical stage 4, $P = 0.038$; **Fig. 2d** and **Supplementary Fig. 6e**). Notably, this signature was found to be independently prognostic in the TCGA LUAD cohort while controlling for other clinical covariates in a Cox proportional-hazards model (hazard ratio (HR) = 1.22; univariate $P = 0.029$, multivariable $P = 0.04$; **Supplementary Table 5**), in which higher enrichment for the signature was associated with significantly worse survival. We also did not detect enrichment for subjects with mutated *TP53* in the cohort correlated with the *KEAP1*-mutant signature. Likewise, we did not observe a significant co-occurrence of subjects with mutant *KEAP1* and mutant *TP53* in the TCGA LUAD cohort ($P = 0.115$). To assess the translational potential of the GEMM results to human *KEAP1*-mutant LUAD, we performed a cross-species comparison of the *Keap1*-mutant transcriptional signatures. The GEMM *Keap1*-mutant signature (**Supplementary Fig. 2i**) was significantly enriched in the human *KEAP1*-mutant signature (**Supplementary Fig. 6f**). Furthermore, the GEMM-based signature could also stratify human patients with significantly different survival times (with correlated patients showing poor survival ($P = 0.003$; **Fig. 2e**)).

Having established the importance of *KEAP1* mutations in mouse and human KRAS-driven LUAD, we sought to uncover potential therapeutic vulnerabilities in this genetic subtype of lung cancer. To this end, we performed a focused CRISPR–Cas9-based genetic screen to identify synthetic genetic interactions with *Keap1* mutations. A pool of lentiviruses expressing a focused CRISPR–Cas9 library was engineered to express sgRNAs against a panel of NRF2 transcriptional targets and genes implicated in the NRF2 antioxidant response (17 genes and 3 control genes, with, 3–4 sgRNAs per gene, for 65 sgRNAs in total; **Fig. 3a**, **Supplementary Table 6**, and **Supplementary Fig. 7a**). We infected KP and KPK cell lines ($n = 2$ per genotype) and assessed the relative depletion of sgRNAs after 14 population doublings to identify genes in which mutations selectively affected the growth of KPK as compared to KP cells in culture (average relative depletion score threshold, $<–0.3$). Notably, out of 60 experimental sgRNAs across 17 genes, three out of four sgRNAs against the *Slc1a5* gene encoding solute carrier family 1 member 5, a glutamine transporter[21], fell below our threshold and were depleted in KPK but not KP cells, suggesting that *Slc1a5* mutation selectively impairs the growth of *Keap1*-mutant cells (**Fig. 3a** and **Supplementary Fig. 7a**). We next generated *Slc1a5*-mutant derivatives of KPK and human lung cancer cells with both *KRAS* and *KEAP1* mutations (A549 and H2030 cells). Upon mutation of *Slc1a5* or *SLC1A5*, these cells displayed markedly decreased growth, whereas we observed no effect of mutation in *Keap1*-WT mouse (KP1, KP2) and *KEAP1*-WT human (H2009) cell lines
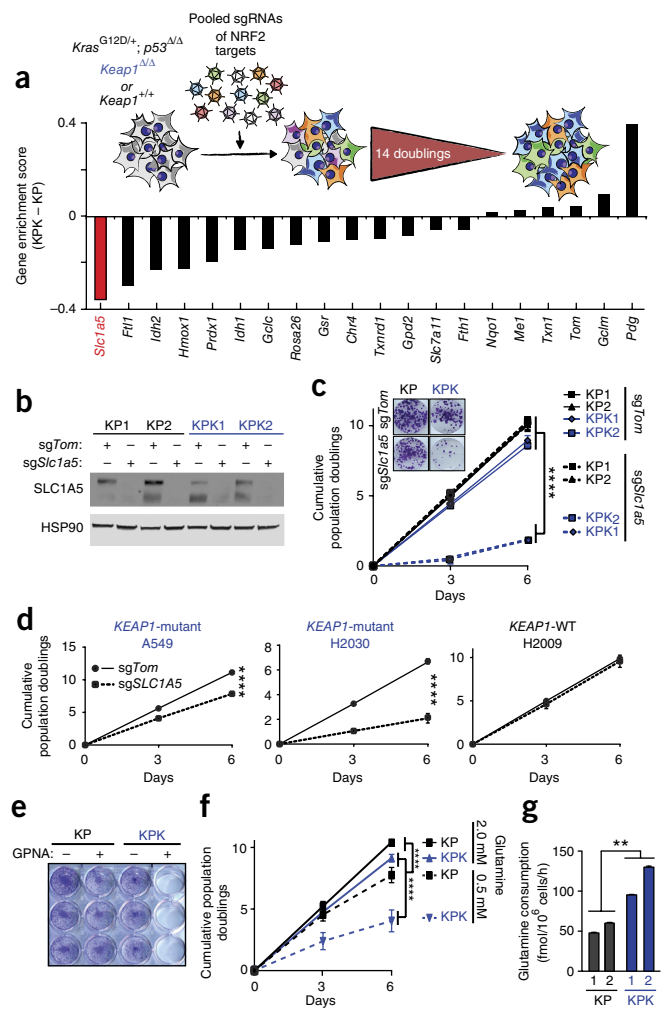

Figure 3 A CRISPR screen reveals that *Keap1*-mutant cells are glycolytic and sensitive to reduced levels of glutamine. (**a**) Pooled sgRNA library screen. Inset, schematic of the experiment. Cells were passaged for 14 population doublings before collection. Bars represent the median differential gene score. A full representation is shown in **Supplementary Figure 7a**. The gene labeled in red had a gene score below our statistical cutoff for gene scores of $<–0.3$. (**b**) Western blot analysis of SLC1A5 in KP and KPK cells infected with sg*Tom* or sg*Slc1a5* following selection. HSP90 was used as a loading control. (**c**) Cumulative population doublings of KP and KPK cells after transduction with sg*Tom*- or sg*Slc1a5*-containing vectors ($n = 4$). Inset, colony-formation assays in KP and KPK cells transduced with sg*Tom* or sg*Slc1a5*. (**d**) Cumulative population doublings of *KRAS*-mutant human lung cancer cell lines that are either WT (H2009) or mutant (A549 and H2030) for *KEAP1* after selection with sg*Tom*- or sg*SLC1A5*-containing vectors ($n = 4$). (**e**) Crystal violet staining of KP and KPK cells treated with 1 mM GPNA or vehicle for 72 h. (**f**) Cumulative population doublings of KP and KPK cells cultured in 2.0 or 0.5 mM glutamine ($n = 4$). (**g**) Glutamine consumption in KP and KPK cell lines ($n = 3$). All samples were normalized to the respective vehicle-treated control. Data are presented as means, with error bars depicting s.e.m. Statistical analyses were performed using two-way ANOVA in **c**, **d**, and **f** and one-way ANOVA with Tukey's *post hoc* test in **g**. $**P < 0.01$, $****P < 0.0001$.

(**Fig. 3b–d** and **Supplementary Fig. 7b**). Furthermore, KPK cell lines were more sensitive to γ-L-glutamyl-*p*-nitroanilide (GPNA), a small-molecule inhibitor of SLC1A5, than KP cell lines (**Fig. 3e** and **Supplementary Fig. 7c**). The selective requirement for SLC1A5 function in KPK cell lines
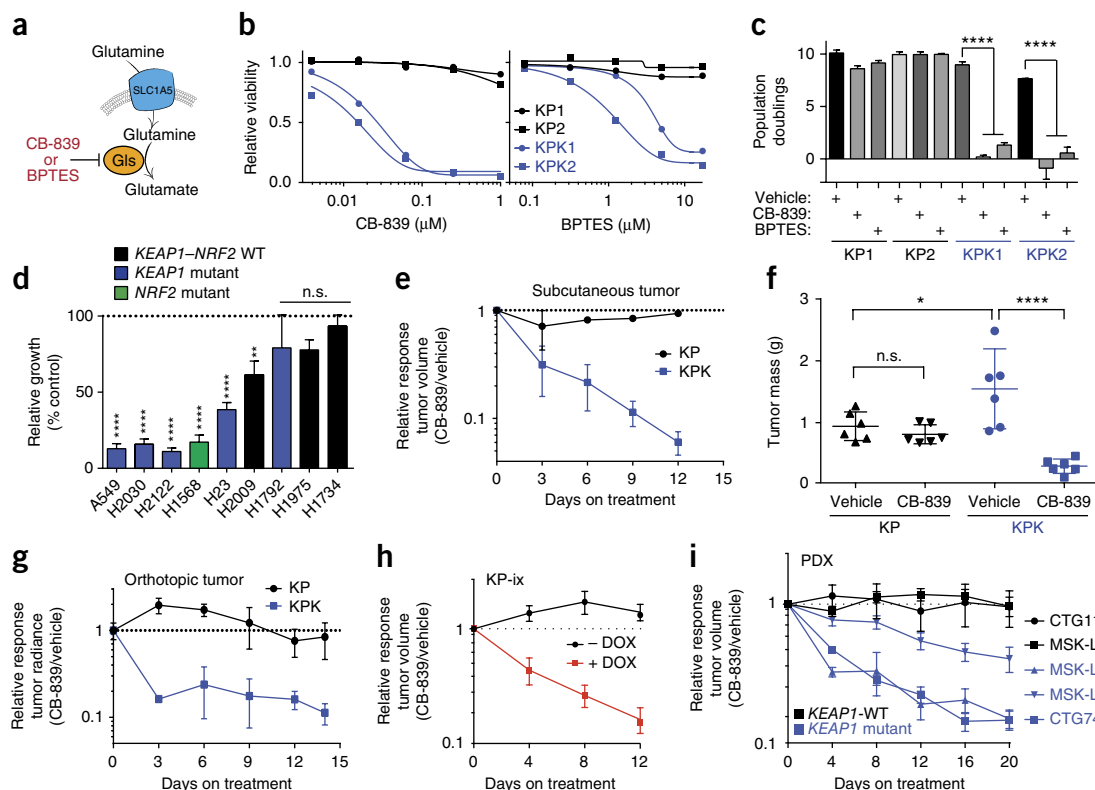
Figure 4 *Keap1*-mutant cells display a robust sensitivity to glutaminase inhibition. (**a**) Schematic of glutamine uptake by SLC1A5 and hydrolysis of glutamine to glutamate by glutaminase (Gls). Inhibitors of glutaminase are shown in red. (**b**) Relative viability assayed by CellTiter-Glo (relative luminescence units) of KP and KPK cells after treatment with CB-839 (left) or BPTES (right) for 72 h. All data points are relative to vehicle-treated controls ($n = 4$ technical replicates per data point). (**c**) Cumulative population doublings of KP and KPK cells in the presence of vehicle, CB-839, or BPTES ($n = 4$ technical replicates per data point) after 6 d in culture. (**d**) Trypan blue exclusion viability counts of indicated human lung cancer cell lines. Each cell line was cultured in the presence of vehicle or 500 nM CB-839 ($n = 4$ technical replicates per cell line). Displayed results are normalized against vehicle-treated cell lines after 72 h of treatment. A549 and H1975 cells harbor WT *TP53*; all other cell lines harbor mutant *TP53*. (**e**,**f**) Subcutaneous tumor volumes of KP and KPK cells treated with vehicle or CB-839 starting from day 13 and measured over time for 25 d ($n = 6$ tumors per genotype per treatment) (**e**) and final masses of those tumors, also shown in **Supplementary Figure 11b** (**f**). (**g**) Orthotopic growth measurements of KP and KPK cells treated with vehicle or CB-839 starting from day 13 ($n = 4$ mice per genotype per treatment). Quantification of luminescence (photon flux) was performed in mice orthotopically transplanted with KP or KPK cells transduced with a vector expressing luciferase. The relative photon flux was calculated by normalizing all time points per mouse to initial measurements at 10 d following transplantation. Individual groups harboring inducible *Nrf2*-GOF cDNA are depicted in **Supplementary Figure 11c**. (**h**) Subcutaneous tumor volumes of KP-ix cells (harboring inducible *Nrf2*-GOF) treated with vehicle or CB-839 in the presence or absence of doxycycline (DOX; $n = 6$ mice per doxycycline treatment group). Individual groups and the full experiment are depicted in **Supplementary Figure 11d**. (**i**) Five PDX models treated with vehicle or CB-839 for the indicated number of days. Individual groups and full experiments are depicted in **Supplementary Figure 11g**,**h**. Data are presented as means, with error bars depicting s.e.m. Statistical analyses were performed using one-way ANOVA with Tukey's *post hoc* test in **c** and **f**, a Student's *t*-test in **d**, and two-way ANOVA in **e** and **g**–**i**. n.s., not significant. *$P < 0.05$, **$P < 0.005$, ****$P < 0.0001$.

suggests a possible metabolic dependency of KPK cells on glutamine. Indeed, decreasing glutamine concentration in the medium led to a robust suppression of growth in KPK cell lines with little effect on KP cell lines (**Fig. 3f** and **Supplementary Fig. 7d**). The dependency of KPK cell lines on SLC1A5 and glutamine could be via fueling of the tricarboxylic acid (TCA) cycle in the context of an increased glycolytic state[22]. In accordance with this possibility, we found that both KPK cell lines had higher glucose (**Supplementary Fig. 7e**) and glutamine (**Fig. 3g**) consumption, coupled with a marked increase in lactate excretion, than KP cells (**Supplementary Fig. 7e**). KPK cells also showed increased sensitivity to the glycolysis inhibitor 2-deoxy-D-glucose (2-DG; **Supplementary Fig. 8a**,**b**). In addition, tracing of a glucose isotopomer in which all six carbons are uniformly ^{13}C ([U^{13}C]glucose) revealed decreased contribution of glucose-derived carbons to TCA cycle intermediates in KPK cells as compared to KP controls (**Supplementary Fig. 8c**–**e**), which was not due to differences in the expression of pyruvate carboxylase (encoded by

Pcx) and glutamine synthetase (encoded by *Glul*) between KPK and KP cells (**Supplementary Table 2**).

We next investigated whether increased glutamine utilization in KPK cell lines could be exploited as a metabolic liability. As glutaminase is the rate-limiting enzyme for glutamine utilization in the cell[14,23] (**Fig. 4a**), we tested two small-molecule inhibitors of glutaminase: *bis*-2-(5-phenylacetamido-1,3,4-thiadiazol-2-*yl*)ethyl sulfide (BPTES) and CB-839 (ref. 23), the latter of which is currently undergoing phase 1 clinical trials for treatment of *KRAS*-mutant lung cancer (**Fig. 4a**,**b** and **Supplementary Fig. 9a**). KPK cells were markedly more sensitive to both drugs than KP cells (**Fig. 4c**). In addition, a panel of human lung cancer cells harboring LOF mutations or GOF mutations in *KEAP1* or *NRF2*, respectively, was sensitive to glutaminase inhibition, whereas *KEAP1*- and *NRF2*-WT cells were largely resistant (**Fig. 4d** and **Supplementary Fig. 9b**). Interestingly, pretreatment of KPK cells with glutamate, pyruvate, or cell-permeable

α-ketoglutarate, but not the antioxidants Trolox or *N*-acetyl cysteine (NAC), rescued sensitivity to CB-839 (**Supplementary Fig. 9c–f**). These results suggest that glutaminase inhibition suppresses cell growth via blocking anaplerosis and not through loss of antioxidant production. To determine whether the sensitivity of KPK cells to glutaminase inhibition was dependent on hyperactive NRF2 signaling, we transduced KP cells with lentiviruses expressing *Nrf2*-GOF (KP-ix; **Supplementary Figs. 3i–o** and **10a,b**). Expression of *Nrf2*-GOF in KP cells led to increased sensitivity to CB-839 (**Supplementary Fig. 10c**). In addition, genetic complementation of *Keap1* in KPK cells reduced NRF2 protein levels, decreased expression of NRF2 target genes, reversed the *in vivo* growth advantage of KPK cells, and rescued the viability of CB-839-treated KPK cells (**Supplementary Fig. 10d–g**).

To investigate the therapeutic potential of targeting glutaminase in *Keap1*-mutant tumors *in vivo*, we transplanted KP and KPK cells subcutaneously and orthotopically (lung) into immunodeficient mice. Once tumors were established, we initiated treatment with either vehicle or CB-839 (**Supplementary Fig. 11a**). In accordance with results from an earlier study[14], we found that KP-derived tumors exhibited no response to CB-839 treatment (**Fig. 4e–g** and **Supplementary Fig. 11b,c**). In contrast, KPK-derived subcutaneous and orthotopic tumors had dramatically decreased growth rates and established smaller final tumor weights in response to CB-839 treatment (**Fig. 4e–g** and **Supplementary Fig. 11b,c**). Furthermore, transplanted KP-ix cells exhibited increased growth upon doxycycline-dependent induction of *Nrf2*-GOF expression, which was suppressed by glutaminase inhibition (**Fig. 4h** and **Supplementary Fig. 11d**). Finally, we demonstrated that glutaminase inhibition suppressed the *in vivo* growth of *KRAS*-driven human LUAD cancer cell lines and patient-derived xenografts (PDXs) with *KEAP1* mutations but had no effect on the growth of *KEAP1*-WT tumors (**Fig. 4i**, **Supplementary Fig. 11e–i**, and **Supplementary Table 7**). Taken together, these data suggest that glutaminase or other targets within this metabolic pathway are attractive therapeutic targets in *KEAP1–NRF2*-mutant LUAD. Furthermore, rational stratification of patients harboring mutations in *KEAP1* and *NRF2* may predict treatment response to glutaminase inhibitors.

In conclusion, we demonstrate that *Keap1* mutations activate the NRF2 antioxidant program and cooperate with mutant *Kras* to drive LUAD progression, supporting the requirement for cancer cells to overcome oxidative stress barriers during tumorigenesis[24–30]. We hypothesize that the metabolic requirement for glutaminolysis in *KEAP1–NRF2*-mutant LUAD tumors may also present a therapeutic vulnerability in other cancers with genetic[31–36], epigenetic[37–39], or post-transcriptional[17] alterations in the *KEAP1–NRF2* pathway. A recent study demonstrated that *KEAP1* loss potentiates resistance to multiple targeted therapies in epidermal growth factor receptor (EGFR)- and RAS-driven cancers, highlighting the value of our therapeutic strategy against *KRAS–KEAP1*-mutant lung cancer[40]. Furthermore, our findings provide unique insight into the therapeutic potential of targeting metabolic dependencies on the basis of somatic variants by combining genetic and metabolic approaches to identify new targets in translational oncology. Collectively, our study presents a new CRISPR–Cas9-based precision medicine platform that can be used to characterize putative cooperating mutations and identify genotype-specific vulnerabilities in cancer.

METHODS

Methods, including statements of data availability and any associated accession codes and references, are available in the online version of the paper.

1. Cox, A.D., Fesik, S.W., Kimmelman, A.C., Luo, J. & Der, C.J. Drugging the undruggable RAS: mission possible? *Nat. Rev. Drug Discov.* **13**, 828–851 (2014).
2. Berger, A.H. *et al.* High-throughput phenotyping of lung cancer somatic mutations. *Cancer Cell* **30**, 214–228 (2016).
3. Cancer Genome Atlas Research Network. Comprehensive molecular profiling of lung adenocarcinoma. *Nature* **511**, 543–550 (2014).
4. Singh, A. *et al.* Dysfunctional KEAP1–NRF2 interaction in non-small-cell lung cancer. *PLoS Med.* **3**, e420 (2006).
5. Itoh, K. *et al.* An Nrf2/small Maf heterodimer mediates the induction of phase II detoxifying enzyme genes through antioxidant response elements. *Biochem. Biophys. Res. Commun.* **236**, 313–322 (1997).
6. Itoh, K. *et al.* Keap1 represses nuclear activation of antioxidant responsive elements by Nrf2 through binding to the amino-terminal Neh2 domain. *Genes Dev.* **13**, 76–86 (1999).
7. Mitsuishi, Y. *et al.* Nrf2 redirects glucose and glutamine into anabolic pathways in metabolic reprogramming. *Cancer Cell* **22**, 66–79 (2012).
8. Harris, I.S. *et al.* Glutathione and thioredoxin antioxidant pathways synergize to drive cancer initiation and progression. *Cancer Cell* **27**, 211–222 (2015).
9. DeNicola, G.M. *et al.* NRF2 regulates serine biosynthesis in non–small cell lung cancer. *Nat. Genet.* **47**, 1475–1481 (2015).
10. Sullivan, L.B., Gui, D.Y. & Heiden, M.G.V. Altered metabolite levels in cancer: implications for tumour biology and cancer therapy. *Nat. Rev. Cancer* **16**, 680–693 (2016).
11. DuPage, M., Dooley, A.L. & Jacks, T. Conditional mouse lung cancer models using adenoviral or lentiviral delivery of Cre recombinase. *Nat. Protoc.* **4**, 1064–1072 (2009).
12. Sánchez-Rivera, F.J. *et al.* Rapid modelling of cooperating genetic events in cancer through somatic genome editing. *Nature* **516**, 428–431 (2014).

13. Mazur, P.K. *et al.* Combined inhibition of BET family proteins and histone deacetylases as a potential epigenetics-based therapy for pancreatic ductal adenocarcinoma. *Nat. Med.* **21**, 1163–1171 (2015).
14. Davidson, S.M. *et al.* Environment impacts the metabolic dependencies of ras-driven non–small cell lung cancer. *Cell Metab.* **23**, 517–528 (2016).
15. Maresch, R. *et al.* Multiplexed pancreatic genome engineering and cancer induction by transfection-based CRISPR/Cas9 delivery in mice. *Nat. Commun.* **7**, 10770 (2016).
16. McKenna, A. *et al.* Whole-organism lineage tracing by combinatorial and cumulative genome editing. *Science* **353**, aaf7907 (2016).
17. Goldstein, L.D. *et al.* Recurrent loss of *NFE2L2* exon 2 is a mechanism for Nrf2 pathway activation in human cancers. *Cell Rep.* **16**, 2605–2617 (2016).
18. Meylan, E. *et al.* Requirement for NF-κB signalling in a mouse model of lung adenocarcinoma. *Nature* **462**, 104–107 (2009).
19. Singh, A. *et al.* RNAi-mediated silencing of nuclear factor erythroid-2–related factor 2 gene expression in non–small cell lung cancer inhibits tumor growth and increases efficacy of chemotherapy. *Cancer Res.* **68**, 7975–7984 (2008).
20. Malhotra, D. *et al.* Global mapping of binding sites for Nrf2 identifies novel targets in cell survival response through ChIP–seq profiling and network analysis. *Nucleic Acids Res.* **38**, 5718–5734 (2010).
21. Hassanein, M. *et al.* SLC1A5 mediates glutamine transport required for lung cancer cell growth and survival. *Clin. Cancer Res.* **19**, 560–570 (2013).
22. Metallo, C.M. *et al.* Reductive glutamine metabolism by IDH1 mediates lipogenesis under hypoxia. *Nature* **481**, 380–384 (2011).
23. Altman, B.J., Stine, Z.E. & Dang, C.V. From Krebs to clinic: glutamine metabolism to cancer therapy. *Nat. Rev. Cancer* **16**, 619–634 (2016).
24. Bauer, A.K. *et al.* Targeted deletion of *Nrf2* reduces urethane-induced lung tumor development in mice. *PLoS One* **6**, e26590 (2011).
25. DeNicola, G.M. *et al.* Oncogene-induced Nrf2 transcription promotes ROS detoxification and tumorigenesis. *Nature* **475**, 106–109 (2011).
26. Satoh, H., Moriguchi, T., Takai, J., Ebina, M. & Yamamoto, M. Nrf2 prevents initiation but accelerates progression through the Kras signaling pathway during lung carcinogenesis. *Cancer Res.* **73**, 4158–4168 (2013).
27. Sayin, V.I. *et al.* Antioxidants accelerate lung cancer progression in mice. *Sci. Transl. Med.* **6**, 221ra15 (2014).
28. Chio, I.I. *et al.* NRF2 promotes tumor maintenance by modulating mRNA translation in pancreatic cancer. *Cell* **166**, 963–976 (2016).
29. Satoh, H. *et al.* NRF2 intensifies host defense systems to prevent lung carcinogenesis, but after tumor initiation accelerates malignant cell growth. *Cancer Res.* **76**, 3088–3096 (2016).
30. Kerr, E.M., Gaude, E., Turrell, F.K., Frezza, C. & Martins, C.P. Mutant *Kras* copy number defines metabolic reprogramming and therapeutic susceptibilities. *Nature* **531**, 110–113 (2016).
31. Cancer Genome Atlas Research Network. Comprehensive genomic characterization of squamous cell lung cancers. *Nature* **489**, 519–525 (2012).
32. Jaramillo, M.C. & Zhang, D.D. The emerging role of the Nrf2–Keap1 signaling pathway in cancer. *Genes Dev.* **27**, 2179–2191 (2013).
33. Konstantinopoulos, P.A. *et al.* Keap1 mutations and Nrf2 pathway activation in epithelial ovarian cancer. *Cancer Res.* **71**, 5081–5089 (2011).
34. Shibata, T. *et al.* Genetic alteration of *Keap1* confers constitutive Nrf2 activation and resistance to chemotherapy in gallbladder cancer. *Gastroenterology* **135**, 1358–1368 (2008).
35. Kim, Y.R. *et al.* Oncogenic *NRF2* mutations in squamous cell carcinomas of oesophagus and skin. *J. Pathol.* **220**, 446–451 (2010).
36. Sato, Y. *et al.* Integrated molecular analysis of clear-cell renal cell carcinoma. *Nat. Genet.* **45**, 860–867 (2013).
37. Fabrizio, F.P. *et al.* Keap1/Nrf2 pathway in kidney cancer: frequent methylation of *KEAP1* gene promoter in clear renal cell carcinoma. *Oncotarget* **8**, 11187–11198 (2017).
38. Muscarella, L.A. *et al.* Regulation of *KEAP1* expression by promoter methylation in malignant gliomas and association with patient's outcome. *Epigenetics* **6**, 317–325 (2011).
39. Hanada, N. *et al.* Methylation of the *KEAP1* gene promoter region in human colorectal cancer. *BMC Cancer* **12**, 66 (2012).
40. Krall, E.B. *et al.* KEAP1 loss modulates sensitivity to kinase targeted therapy in lung cancer. *eLife* **6**, e18970 (2017).

ONLINE METHODS

Mice. All mouse experiments described in this study were approved by the Massachusetts Institute of Technology Institutional Animal Care and Use Committee (IACUC). LSL-*Kras*[G12D]; *Trp53*[flox] mice have already been described[41,42]. For all mouse studies, >3 mice were used for each experimental cohort per specified genotype. All mice were maintained on a mixed C57BL/6–129/Sv genetic background. Total tumor burden and grading analyses were conducted on >3 mice per genotype. No mice were excluded from analyses. Mice with the appropriate genotype aged 6–8 weeks were randomly selected to begin tumor initiation studies with pSECC-sg*Tom* or pSECC-sg*Keap1*. Mice were infected intratracheally with lentiviruses as described[11]. The total lung area occupied by each tumor was measured on H&E-stained slides using NIS-Elements software (Nikon). All tumor burden and IHC analyses were done in a blinded fashion, in which the researcher was unaware of which genotype the samples had.

Cell culture. Parental cell lines from KP[43] and LKR[18] mice were previously established and described. Human cell lines were acquired from the American Type Culture Collection (ATCC). All lines tested negative for mycoplasma. Cells were maintained in DMEM or RPMI supplemented with 10% FBS and gentamicin. Cell lines expressing reverse tetracycline–controlled transactivator (rtTA) were kept under neomycin selection (400 μg/ml). Cell lines expressing doxycycline-inducible NRF2 constructs remained under hygromycin selection (600 μg/ml). Cells were treated with inhibitors D,L-sulforaphane (SFN; EMD Millipore Calbiochem), dimethyl fumarate (DMF; Sigma-Aldrich), L-buthionine-sulfoximine (BSO; Sigma-Aldrich), auranofin (AUR; Tocris bioscience), erastin (ERA; Sigma-Aldrich), GPNA (Sigma-Aldrich), 2-deoxy-D-glucose (2DG; Acros Organics), BPTES (Sigma-Aldrich), and CB-839 (provided by C.J. Thomas) and antioxidants or metabolites Trolox (Acros Organics), *N*-acetyl-L-cysteine (NAC; Sigma-Aldrich), 6 mM glutamate (Sigma-Aldrich), 2 mM pyruvate (Gibco), and 2 mM dimethyl-2-oxoglutarate (DMG; Sigma-Aldrich). Cell viability in the presence of all compounds was assessed by CellTiter-Glo (Promega, catalog no. G7570) and trypan blue exclusion on a Countess II Automated Cell Counter (Life Technologies). For clonogenic and low-density assays, cells were stained with crystal violet solution (25% methanol in water). To determine cell counts after DMF treatment, cells were fixed with 4% paraformaldehyde for 15 min at 4 °C. Cells were then washed in ice-cold PBS and stained with Hoechst DNA stain. Plates were quantified using an Infinite 200 PRO plate reader (Tecan) or a SpectraMax M5e microplate reader (Molecular Devices).

Focused CRISPR–Cas9 genetic screen. Oligonucleotides for sgRNAs were synthesized by Integrated DNA Technologies, annealed *in vitro*, and inserted into lentiCRISPR-V244. Cloned products were then transformed into *Escherichia coli* 10G SUPREME Electrocompetent Cells (Lucigen). This plasmid pool was used to generate lentivirus-containing supernatants. The titer of lentiviral supernatants was determined by infecting target cells with several amounts of virus in the presence of polybrene (8 μg/ml; Millipore, catalog no. TR-1003-G), counting the number of drug-resistant infected cells after 3 d of selection. KP and KPK cells were infected at a multiplicity of infection (MOI) of ~0.5 and selected with puromycin (3 μg/ml) 72 h after infection. An initial pool of cells was harvested for genomic DNA extraction. The remaining cells were cultured for 14 doublings, after which cells were harvested for genomic DNA extraction. sgRNA inserts were PCR amplified and then purified and sequenced on a MiSeq instrument (Illumina) according to prior studies[44]. Sequencing reads were mapped, and the abundance of each sgRNA was tallied. Gene score is defined as the median $\log_2$ fold change in abundance between the initial and final populations for all sgRNAs targeting the gene. The differential gene score is the difference between the KP and KPK cell gene scores.

Immunoblotting. Cells were lysed in 250 μl of ice-cold RIPA buffer (Pierce, catalog no. 89900) supplemented with 1× cOmplete Mini inhibitor mixture (Roche, catalog no. 11 836 153 001) and mixed on a rotator at 4 °C for 30 min. The protein concentration of the cell lysates was quantified using the Bio-Rad DC Protein Assay (catalog no. 500-0114). 50–80 μg of total protein was separated on 4–12% Bis-Tris gradient gels (Bio-Rad) by SDS–PAGE and then transferred to nitrocellulose membranes. The following antibodies were used for immunoblotting: anti-Flag (Sigma, F1804, 1:1,000), anti-GAPDH (Santa Cruz, sc-25778, 1:500), anti-Hsp90 (BD, catalog no. 610418, 1:10,000), anti-Nrf2 (Santa Cruz, sc-722, 1:200 and custom antibody provided by E.E.S. at 1:200), anti-Keap1 (CST, catalog no. 8047, 1:1,000), anti-Gclc (Santa Cruz, sc-22755, 1:200), anti-Slc1a5 (Santa Cruz, ASCT2 (M-63) sc-99003, 1:100), anti-Txnrd1 (Abcam, ab124954, 1:1,000), and anti-p53 (CST, 2524S lot 12, 1:1,000).

Immunohistochemistry and immunofluorescence. Mice were euthanized by carbon dioxide asphyxiation. Lungs were perfused through the trachea with 4% paraformaldehyde, fixed overnight, transferred to 70% ethanol, and subsequently embedded in paraffin. Sections were cut at a thickness of 4 μm and stained with H&E for pathological examination. Chromogenic IHC was performed on a Ventana Medical Systems DISCOVERY XT instrument with online deparaffinization using Ventana's reagents and detection kits and antigen retrieved in Ventana Cell Conditioner 1 or 2. The following antibodies were used for IHC: anti-pHH3 (Ser10; Cell Signaling, 9701, 1:200), anti-Ki-67 (Spring Bioscience, catalog no. M3062, 1:400), anti-Nqo1 (Sigma-Aldrich, HPA007308, 1:100), anti-Nrf2 (provided by the laboratory of E.E.S., 1:100), and anti-8-oxo-dg (Abcam, ab48508, N45.1, 1:200). HRP detection was used for NQO1, NRF2, pHH3, and Ki-67. Alkaline phosphatase (AP) detection was used for 8-oxo-dG and was visualized with Fast Red chromogen. Antigen retrieval for NQO1 and NRF2 was performed in a Ventana Cell Conditioner 1 (TBE). Antigen retrieval was performed with a Ventana Cell Conditioner 2 (citrate) for 8-oxo-dG, Ki-67, and pHH3. Pictures were obtained using a Nikon 80i microscope with a DS-U3 camera and NIS-Elements software and with a digital whole-slide scanner (Leica, SCN400F) and Slidepath software version 4.0.8.

Genomic DNA isolation. Genomic DNA from entire snap-frozen left lung lobes or microdissected tumors was isolated using the High Pure PCR Template Preparation Kit (Roche, catalog no. 11796828001) following the manufacturer's guidelines. PCR products for MiSeq (**Supplementary Table 8**) were amplified using Herculase II Fusion DNA polymerase (Agilent, catalog no. 600679) (see **Supplementary Table 8** for the primers used for genomic DNA isolation).

Lentiviral production. Lentiviruses were produced by cotransfection of HEK293 cells with lentiviral backbone constructs and packaging vectors (delta8.2 and VSV-G) using TransIT-LT1 (Mirus Bio, catalog no. MR 2306). Supernatant was collected 48 and 72 h following transfection and concentrated by ultracentrifugation at 106,750*g* for 90 min, and viruses were resuspended in an appropriate volume of Opti-MEM (Gibco, catalog no. 31985-062).

Lentiviral vectors and sgRNA cloning. The pSECC lentiviral vector and cloning strategy were previously described[11]. For CRISPR experiments, the lentiCRISPR-V2 lentiviral vector was used[45]. For sgRNA cloning, the lentiC-RISPR-V2 vector was digested with BsmBI and ligated with BsmBI-compatible annealed oligonucleotides for sgRNAs (**Supplementary Table 8**).

Tumor purity correction. Lung lobe and microdissected tumor genomic DNA was used to perform real-time PCR–based analysis to detect relative levels of the non-recombined LSL-*Kras*[G12D] allele using forward primer 5′-CTCTTGCCTACGCCACCAGCTC-3′ and reverse primer 5′-AGCTAGCCACCATGGCTTGAGTAAGTCTGCA-3′. To correct for DNA loading of each sample, we amplified chr. 5: 10054507–10054621 using forward primer 5′-GAAGAAATTAGAGGGCATGCTTC-3′ and reverse primer 5′-CTTCTCCCAGTGACCTTATGTA-3′. Real-time PCR was performed using KAPA Fast SYBR master mix in a Roche LightCycler Real-Time PCR instrument. To calculate percentage purity, we performed the following calculations for each sample: $\Delta\Delta Cp$ (tumor X) = Cp (chr. 5) − Cp (LSL-*Kras*[G12D]) to normalize for sample loading and then calculated $1/\Delta\Delta\Delta\Delta Cp = (\Delta\Delta Cp$ (tumor X) − $\Delta\Delta Cp$ (lung control)) for each sample where Cp is the crossing point, the point at which the amplification curve crosses the vertical threshold line.

Transcriptome analysis. RNA was collected from cells as before[46] with the RNeasy Plus Mini Kit (Qiagen). For real-time qPCR analysis, cDNA was synthesized from RNA with the High Capacity cDNA Reverse Transcription Kit (Applied Biosystems, catalog no. 4368814). Genes *Slc7a11*, *Gclc*, *Hmox1*, and *Nqo1* were analyzed by qRT–PCR on a LightCycler 480 II (Roche). RT–qPCR primers are listed in **Supplementary Table 8**.

Glutaminase inhibitor. Mice were treated as before with 200 mg per kg body weight CB-839 or vehicle twice a day after the tumor-establishment phase. The vehicle control contained 25% (w/v) 2-hydroxypropyl-β-cyclodextrin in 10 mM citrate (pH 2.0), and CB-839 was formulated at 20 mg/ml for a final dosing volume of 10 ml per kg body weight.

Extracellular flux measurements. Extracellular flux measurements were calculated by extracting fresh and spent medium supernatants from tracing experiments after 24 h of growth. Cells were assumed to grow exponentially over the culture period. Glucose, lactate, and glutamine were measured using a YSI biochemistry analyzer (Yellow Springs Instruments, Yellow Springs, OH).

Reactive oxygen species and glutathione. ROS in cultured cells were measured by incubating 1×10^6 cells with 5 μM CM-H$_2$DCFDA (C6827, Life Technologies) for 30 min at 37 °C. 5-carboxy-2′,7′-dichlorodihydrofluorescein (DCF) fluorescence was acquired on the Attune NxT Flow Cytometer (Thermo Fisher) and analyzed using FlowJo software (Tree Star). Reduced and oxidized glutathione (GSH and GSSG, respectively) were measured with a GSH/GSSG-Glo Assay kit (V6611, Promega) for the indicated amount of time.

Statistics. For statistical analyses, we used GraphPad Prism software v.6.03, and variance was similar between the groups that were compared: *P* values were determined by Student's *t*-test for all measurements of tumor burden and IHC quantifications except for the contingency tables, in which Fisher's exact test or the chi-squared test was used. One-way ANOVA with Tukey's *post hoc* test was used for comparisons between multiple groups; for analysis between groups over multiple time measurements (growth curves), two-way ANOVA was used. Figure legends specify the statistical analysis used. Standardized half-maximal inhibitory concentration (IC$_{50}$) values for the heat map in **Supplementary Figure 3a** were calculated as follows: $z = (X - \mu)/\sigma$, where z is the z-score, X is the 'score' or raw value, μ is the mean of the population, and σ is the standard deviation of the population. Subject co-occurrence was assessed using Fisher's exact test, and enrichment was assessed using the hypergeometric test. All error bars denote s.e.m. Detailed information on experimental design and reagents can be found in the **Life Sciences Reporting Summary** accompanying this manuscript.

Bioinformatic analyses of CRISPR-targeted loci. For libraries prepared with the Nextera DNA Library Preparation Kit, Illumina MiSeq reads were trimmed to 120 bp after reviewing base-quality profiles in order to drop lower-quality 3′ ends. Traces of Nextera adaptors were clipped using the FASTX-Toolkit (Hannon Lab, CSHL), and pairs with each read greater than 15 bp in length were retained. Additionally, read pairs in which either read had 50% or more bases below a base-quality threshold of Q30 (Sanger) were dropped from subsequent analyses. For PCR amplicons (sequenced at the MGH sequencing facility), 142-bp paired-end reads were used in downstream analyses. The reference sequence of the target locus was supplemented with 10-bp genomic flanking sequences and was indexed using an enhanced suffix array[47]. Read ends were anchored in the reference sequence using 10-bp terminal segments for a suffix array index lookup to search for exact matches. A sliding window of unit step size and a maximal soft-clip limit of 10 bp were used to search for possible anchors at either end of each read. For each read, optimal Smith–Waterman dynamic programming alignment[48] was performed between the reduced state space of the read sequence and the corresponding reference sequence spanning the maximally distanced anchor locations. Scoring parameters were selected to allow for sensitive detection of short and long indels while allowing for up to four mismatches, and the highest scoring alignment was selected. Read pairs with both reads aligned in the proper orientation were processed to summarize

the number of wild-type reads and the location and size of each indel event. Overlapping reads within pairs were both required to support the event if they overlapped across the event location. Additionally, mutation events and wild-type reads were summarized within the extents of the sgRNA sequence and protospacer adjacent motif (PAM) site by considering read alignments that had a minimum of 20-bp overlap with this region. Mutation calls were translated to genomic coordinates and subsequently annotated using ANNOVAR[49]. The alignment and post-processing code was implemented in C++ along with library functions from SeqAn[50] and SSW and utility functions in Perl and R (http://www.R-project.org/). Mutation calls were subjected to manual review using the Integrated Genomics Viewer (IGV)[51].

New York University targeted exome capture sequencing. All protein-coding exons for the genes of interest were sequenced using the following methodology. 500 ng of DNA from each sample was sheared to an average of 150 bp in a Covaris instrument for 360 s (duty cycle, 10%; intensity, 5; cycles/burst, 200). Barcoded libraries were prepared using the KAPA Low-throughput Library Preparation Kit Standard (KAPA Biosystems). Libraries were amplified using the KAPA HiFi Library Amplification kit (KAPA Biosystems) (8 cycles) and quantified using Qubit Fluorimetric Quantitation (Invitrogen) and Agilent Bioanalyzer. An equimolar pool of 24 barcoded libraries was used as input for hybridization-based capture using one reaction. The xGen Lockdown predesigned probes (Integrated DNA Technologies) targeted coding exons of the genes of interest. Capture by hybridization was performed according to the IDT protocol. The final pooled capture libraries were quantified by Qubit (Invitrogen) and Bioanalyzer (Agilent) and sequenced on an Illumina HiSeq 4000 as paired-end 150-bp reads.

Methods for lung cancer sample collection. Eighty-eight primary lung cancers were collected along with matching blood mononuclear cells and remote normal lung samples, which were snap frozen in liquid nitrogen at the time of resection. DNA extractions were performed (Qiagen, Dusseldorf, Germany) for targeted exome capture, and matching formalin-fixed paraffin-embedded (FFPE) tissue was used for NQ01 staining. All use of human tissue and body fluids was approved under New York University Institutional Review Board protocol 8896.

Human exome data analyses. Sequencing results were demultiplexed and converted to FASTQ format using Illumina bcl2fastq software. The reads were adaptor and quality trimmed with Trimmomatic[52] and then aligned to the human genome (build hg19/GRCh37) using the Burrows–Wheeler Aligner with the BWA-MEM algorithm[53]. Duplicate reads were removed using Sambamba[54]. Further local indel realignment and base-quality score recalibration were performed using the Genome Analysis Toolkit (GATK)[55]. Single-nucleotide and small indel somatic variants were called with MuTect2 (ref. 56). ANNOVAR[49] was used to annotate variants with functional consequence on genes as well as to identify the presence of genes in dbSNP, the Exome Aggregation Consortium (ExAC), the 1000 Genomes project, and the Catalog of Somatic Mutations in Cancer (COSMIC).

Allograft, xenograft, and patient-derived xenograft experiments. For allograft experiments, cells derived from mouse lung tumors were transplanted subcutaneously (1×10^6 cells) under the skin or orthotopically (2.5×10^5 cells) in the lung of nude (*Foxn1^{nu}*) or NOD-SCID-gamma (NSG; NOD.Cg-*Prkdc^{scid}Il2rg^{tm1Wjl}*/SzJ) mice. For xenograft experiments, human lung cancer cell lines (1×10^6 cells) were transplanted subcutaneously into NSG mice with a 1:1 ratio of Matrigel. PDXs were revived and passaged once in NSG mice, and a live 2×2 mm piece of tumor was surgically transplanted subcutaneously into recipient NSG mice under anesthesia. After 6 weeks of recovery and engraftment, mice harboring tumors with volumes of 25–100 mm^3 were randomized to receive vehicle or CB-839. Details on the generation of PDXs have been previously described[57]. Memorial Sloan Kettering–Integrated Mutation Profiling of Actionable Cancer Targets (MSK-IMPACT)[58] was performed on xenografts after mouse stroma depletion, and mutations were called against matched normal blood samples as previously detailed[59]. Subcutaneous tumor volumes were calculated according to the following formula: volume

$(mm^3) = (a_2 \times b) \times (\pi/6)$, in which a is the smaller dimension and b is the larger dimension.

Human clinical data analyses. Genomic data for samples from subjects with lung adenocarcinoma ($n = 548$) were obtained from TCGA LUAD (http://cancergenome.nih.gov/). This included RNA-seq gene expression profiles of primary tumor samples from subjects ($n = 488$), mutation calls, and associated clinical data ($n = 458$ subjects with RNA-seq data for primary tumors with associated survival data). Individual sample expression profiles were scored with gene expression signatures using ssGSEA[60,61]. Patients were stratified into equal top and bottom percentile sets according to their correlation score (or the top-scoring percentage versus the rest of the cohort). Kaplan–Meier survival analyses were conducted between these sets of subjects, and the log-rank test was used to assess significance. The mouse-derived *Keap1*-mutant signature was similarly used to perform Kaplan–Meier survival analyses after translation of mouse gene names to human nomenclature (http://www.genenames.org/). Additionally, the Cox proportional hazards regression model was used to analyze the prognostic value of the human-derived *KEAP1*-mutant signature across all subjects within the TCGA LUAD cohort in the context of additional clinical covariates. All univariate and multivariable analyses were conducted within a 5-year survival timeframe. The following subject and tumor-stage clinical characteristics were used: signature (*KEAP1*-mutant signature strong versus weak correlation); sex (male versus female); age (years, continuous); smoking history (reformed > 15 y versus nonsmoker, reformed < 15 y versus nonsmoker, current smoker versus nonsmoker); Union for International Cancer Control (UICC) tumor nodes metastasis (TNM) stage specification (stage 3 or 4 versus 1 or 2); UICC *T*-score specification (T2 versus T1, T3 or T4 versus T1); UICC *N*-score specification (N1 or N2 versus N0). Hazard ratio proportionality assumptions for the Cox regression model were validated by testing for all interactions simultaneously ($P = 0.723$). Interactions between the *KEAP1*-mutant signature and TNM stage, T score, and N score (significant covariates in the model) were tested using a likelihood-ratio test (LRT) to contrast a model consisting of both covariates with another model consisting of both covariates plus an interaction term. No statistically significant difference was found between the two models (TNM: $P = 0.445$; T score: $P = 0.455$; N score: $P = 0.494$; likelihood-ratio test). To test for statistically significant associations between the *KEAP1*-mutant signature correlation scores and TCGA LUAD TNM stage (stages 1–4) and grade levels (*T*-scores), the Kurskal–Wallis test was used to assess overall significance, and the Kolmogorov–Smirnov test was used to assess pairwise differences. Results were visualized using empirical cumulative distribution function (ECDF) plots. All statistical analyses were conducted in R (http://www.R-project.org/), and all survival analyses were conducted using the survival package in R[47].

NRF2 core target signature. Three published data sets were used to derive a high-confidence 108-gene signature of NRF2-induced targets. Normalized microarray expression data for GSE38332 (ref. 62) were downloaded from the Gene Expression Omnibus (GEO). Differential expression analysis using R/limma[63] was performed to identify genes that were differentially regulated between control and *Nrf2* siRNA–treated samples. A list of NRF2-induced genes ($n = 433$) was identified using thresholds of false discovery rate (FDR) < 0.05 and fold change < 1.5. NRF2 targets ($n = 345$) derived by Mitsuishi *et al.*[7] from microarray analyses of A549 cells treated with *Nrf2* siRNA versus a control siRNA were used as the second data set (**Supplementary Table 1** from ref. 7). High-confidence NRF2 targets ($n = 244$) derived by Malhotra *et al.*[20] from integrated analyses of microarray gene expression and chromatin immunoprecipitation and sequencing (ChIP–seq) data were used as the third data set (**Supplementary Table 5** from ref. 20). All nonhuman gene names were mapped to human gene equivalents where needed. Genes that overlapped between two or more data sets were included in the high-confidence NRF2 core target signature and used in downstream analyses (**Supplementary Table 3**). Differential gene expression analyses were conducted in R.

Gene expression signature analyses. Illumina HiSeq 2000 50-nt single-end reads were mapped to the UCSC mm9 mouse genome build (http://genome.ucsc.edu/) using RSEM[64]. Raw estimated expression counts were upper-quartile

normalized to a count of 1,000 (ref. 65). *Keap1*-mutant ($n = 2$), wild-type ($n = 2$), and wild-type plus SFN-treated ($n = 2$) samples were jointly analyzed to derive a mouse signature for *Keap1*-mutant gene expression changes. Given the complexity of the database in terms of a mixture of genotypes and treatment, a high-resolution signature-discovery approach (Independent Component Analysis (ICA)) was employed to characterize global gene expression profiles, as described previously[43,46,66]. This unsupervised blind source separation technique was used on this discrete count-based expression data set to elucidate statistically independent and biologically relevant signatures. ICA is a signal-processing and multivariate data analysis technique in the category of unsupervised matrix factorization methods. Conceptually, ICA decomposes the overall expression data set into independent signals (gene expression patterns) that represent distinct signatures. High-ranking positively and negatively correlated genes in each signature represent gene sets that drive the corresponding expression pattern (in either direction). Each signature is thus two-sided, allowing for identification of upregulated and downregulated genes for each signature within each sample. Formally, using input data consisting of a genes–samples matrix, ICA uses higher-order moments to characterize the data set as a linear combination of statistically independent latent variables. These latent variables represent independent components based on maximizing non-Gaussianity and can be interpreted as independent source signals that have been mixed together to form the data set under consideration. Each component includes a weight assignment to each gene that quantifies its contribution to that component. Additionally, ICA derives a mixing matrix that describes the contribution of each sample toward the signal embodied in each component. This mixing matrix can be used to select signatures among components with distinct gene expression profiles across the set of samples. The R implementation of the core algorithm Joint Approximate Diagonalization of Eigenmatrices (JADE) algorithm[67] was used along with custom R utilities. Statistical significance of biologically relevant signatures was assessed using the Mann–Whitney–Wilcoxon test ($\alpha = 0.05$). A mouse *Keap1*-mutant signature was derived from this analysis, identifying genes with a differential expression pattern between the wild-type sample and all other samples. Genes from the resulting signature with $|z\text{-score}| > 2$ were used in subsequent Kaplan–Meier and Cox regression survival analyses. Similarly, expression profiles from the TCGA human lung adenocarcinoma cohort were analyzed to derive a *KEAP1*-mutant gene expression signature. Using mutation calls from TCGA (MAF files), primary tumor samples from subjects with protein-altering mutations in *KEAP1* ($n = 79$) and wild-type *KEAP1* ($n = 380$) were identified. A combined data set of these samples was analyzed (using ICA) to detect a statistically significant expression pattern (Mann–Whitney–Wilcoxon test) separating mutant from wild-type samples. Genes from the resulting signature with $|z\text{-score}| > 2$ were used in subsequent Kaplan–Meier and Cox regression survival analyses. All RNA-seq analyses were conducted in the R statistical programming language (http://www.r-project.org/). Gene set enrichment analysis (GSEA) was carried out using the pre-ranked mode with default settings[61].

Gas chromatography–mass spectrometry analysis of glucose-traced metabolites. 2×10^5 cells were seeded in 2 ml of RPMI-1640 in six-well plates. The medium was then replaced with 2 ml of fresh RPMI-1640 containing 11 mM [U-^{13}C]D-glucose. Cells were cultured for 24 h to reach steady-state labeling of TCA cycle intermediates. Cells were washed 1× in ice-cold saline and then collected by scraping in 600 µl of 80% (v/v) ice-cold methanol containing 1.4 µg/ml norvaline (Sigma-Aldrich). Samples were vortexed for 10 min at 4 °C and then centrifuged at max speed for 10 min. Supernatant was transferred to fresh tubes and then dried under nitrogen. Dried and frozen metabolite extracts were derivatized with 16 µl of methoxamine (MOX) reagent (Thermo Fisher) for 60 min at 37 °C and *N*-tertbutyldimethylchlorosilane (Sigma-Aldrich) for 30 min at 60 °C. After derivatization, samples were analyzed by gas chromatography–mass spectrometry (GC–MS) using a DB-35ms column (Agilent Technologies) in an Agilent 7890A gas chromatograph coupled to an Agilent 5997B mass spectrometer. Helium was used as the carrier gas at a flow rate of 1.2 ml/min. One microliter of sample was injected in split mode (split 1:1) at 270 °C. After injection, the GC oven was held at 100 °C for 1 min and then increased to 300 °C at 3.5 °C/min. The oven was then ramped to 320 °C at

20 °C/min and held for 5 min at 320 °C. The MS system operated under electron impact ionization at 70 eV, and the MS source and quaddrupole were held at 230 °C and 150 °C, respectively. The detector was used in scanning mode, and the scanned ion range was 10–650 m/z. Mass isotopomer distributions were determined by integrating appropriate ion fragments for each metabolite[68] using in-house software[69] that corrects for natural abundance using previously described methods[70].

Data availability. Data from this study are available from the corresponding author upon reasonable request. All sequence data sets are available under BioProject PRJNA400522. Uncropped immunoblots are available in **Supplementary Figure 12**. A **Life Sciences Reporting Summary** for this paper is available.

41. Jackson, E.L. *et al.* Analysis of lung tumor initiation and progression using conditional expression of oncogenic K-*ras*. *Genes Dev.* **15**, 3243–3248 (2001).
42. Jackson, E.L. *et al.* The differential effects of mutant p53 alleles on advanced murine lung cancer. *Cancer Res.* **65**, 10280–10288 (2005).
43. Dimitrova, N. *et al.* Stromal expression of miR-143/145 promotes neoangiogenesis in lung cancer development. *Cancer Discov.* **6**, 188–201 (2016).
44. Sanjana, N.E., Shalem, O. & Zhang, F. Improved vectors and genome-wide libraries for CRISPR screening. *Nat. Methods* **11**, 783–784 (2014).
45. Shalem, O. *et al.* Genome-scale CRISPR–Cas9 knockout screening in human cells. *Science* **343**, 84–87 (2014).
46. Papagiannakopoulos, T. *et al.* Circadian rhythm disruption promotes lung tumorigenesis. *Cell Metab.* **24**, 324–331 (2016).
47. Abouelhoda, M.I., Kurtz, S. & Ohlebusch, E. Replacing suffix trees with enhanced suffix arrays. *J. Discrete Algorithms (AMST)* **2**, 53–86 (2004).
48. Smith, T.F. & Waterman, M.S. Identification of common molecular subsequences. *J. Mol. Biol.* **147**, 195–197 (1981).
49. Wang, K., Li, M. & Hakonarson, H. ANNOVAR: functional annotation of genetic variants from high-throughput sequencing data. *Nucleic Acids Res.* **38**, e164 (2010).
50. Döring, A., Weese, D., Rausch, T. & Reinert, K. SeqAn an efficient, generic C. library for sequence analysis. *BMC Bioinformatics* **9**, 11 (2008).
51. Thorvaldsdóttir, H., Robinson, J.T. & Mesirov, J.P. Integrative Genomics Viewer (IGV): high-performance genomics data visualization and exploration. *Brief. Bioinform.* **14**, 178–192 (2013).
52. Bolger, A.M., Lohse, M. & Usadel, B. Trimmomatic: a flexible trimmer for Illumina sequence data. *Bioinformatics* **30**, 2114–2120 (2014).
53. Li, H. & Durbin, R. Fast and accurate short read alignment with Burrows–Wheeler transform. *Bioinformatics* **25**, 1754–1760 (2009).
54. Tarasov, A., Vilella, A.J., Cuppen, E., Nijman, I.J. & Prins, P. Sambamba: fast processing of NGS alignment formats. *Bioinformatics* **31**, 2032–2034 (2015).
55. DePristo, M.A. *et al.* A framework for variation discovery and genotyping using next-generation DNA sequencing data. *Nat. Genet.* **43**, 491–498 (2011).
56. Cibulskis, K. *et al.* Sensitive detection of somatic point mutations in impure and heterogeneous cancer samples. *Nat. Biotechnol.* **31**, 213–219 (2013).
57. Gardner, E.E. *et al.* Chemosensitive relapse in small cell lung cancer proceeds through an EZH2–SLFN1L axis. *Cancer Cell* **31**, 286–299 (2017).
58. Cheng, D.T. *et al.* Memorial Sloan Kettering–Integrated Mutation Profiling of Actionable Cancer Targets (MSK-IMPACT): a hybridization capture-based next-generation sequencing clinical assay for solid tumor molecular oncology. *J. Mol. Diagn.* **17**, 251–264 (2015).
59. Schneeberger, V.E., Allaj, V., Gardner, E.E., Poirier, J.T. & Rudin, C.M. Quantitation of murine stroma and selective purification of the human tumor component of patient-derived xenografts for genomic analysis. *PLoS One* **11**, e0160587 (2016).
60. Barbie, D.A. *et al.* Systematic RNA interference reveals that oncogenic KRAS-driven cancers require TBK1. *Nature* **462**, 108–112 (2009).
61. Subramanian, A. *et al.* Gene set enrichment analysis: a knowledge-based approach for interpreting genome-wide expression profiles. *Proc. Natl. Acad. Sci. USA* **102**, 15545–15550 (2005).
62. Singh, A. *et al.* Transcription factor NRF2 regulates miR-1 and miR-206 to drive tumorigenesis. *J. Clin. Invest.* **123**, 2921–2934 (2013).
63. Ritchie, M.E. *et al.* limma powers differential expression analyses for RNA-sequencing and microarray studies. *Nucleic Acids Res.* **43**, e47 (2015).
64. Li, B. & Dewey, C.N. RSEM: accurate transcript quantification from RNA-Seq data with or without a reference genome. *BMC Bioinformatics* **12**, 323 (2011).
65. Bullard, J.H., Purdom, E., Hansen, K.D. & Dudoit, S. Evaluation of statistical methods for normalization and differential expression inmRNA-Seq experiments. *BMC Bioinformatics* **11**, 94(2010).
66. Li, C.M. *et al.* Foxa2 and Cdx2 cooperate with Nkx2-1 to inhibit lung adenocarcinoma metastasis. *Genes Dev.* **29**, 1850–1862 (2015).
67. Biton, A. *et al.* Independent component analysis uncovers the landscape of the bladder tumor transcriptome and reveals insights into luminal and basal subtypes. *Cell Rep.* **9**, 1235–1245 (2014).
68. Lewis, C.A. *et al.* Tracing compartmentalized NADPH metabolism in the cytosol and mitochondria of mammalian cells. *Mol. Cell* **55**, 253–263 (2014).
69. Young, J.D., Walther, J.L., Antoniewicz, M.R., Yoo, H. & Stephanopoulos, G. An elementary metabolite unit (EMU) based method of isotopically nonstationary flux analysis. *Biotechnol. Bioeng.* **99**, 686–699 (2008).
70. Fernandez, C.A., Des Rosiers, C., Previs, S.F., David, F. & Brunengraber, H. Correction of ^{13}C mass isotopomer distributions for natural stable isotope abundance. *J. Mass Spectrom.* **31**, 255–262 (1996).

nature research

Corresponding author(s): Tyler Jacks
Thales Papagiannakopoulos

☐ Initial submission ☐ Revised version ☒ Final submission

Life Sciences Reporting Summary

Nature Research wishes to improve the reproducibility of the work that we publish. This form is intended for publication with all accepted life science papers and provides structure for consistency and transparency in reporting. Every life science submission will use this form; some list items might not apply to an individual manuscript, but all fields must be completed for clarity.

For further information on the points included in this form, see Reporting Life Sciences Research. For further information on Nature Research policies, including our data availability policy, see Authors & Referees and the Editorial Policy Checklist.

▶ Experimental design

1. Sample size

Describe how sample size was determined.

Sample sizes for each experiment are outlined in the figure itself or in the figure legend. For all Experiments at least 3 or more replicates/number of animals was used in order to obtain statistical significance.

For all animal studies, >3 animals were used for each experimental cohort per specified genotype. Total burden, and grading analysis were conducted on <3 mice per genotype.

2. Data exclusions

Describe any data exclusions.

We have excluded data for an independently derived KEAP1-mutant signature, which we have included for the reviewers only to directly answer their question regarding this signature.

No animals were excluded from the analysis

3. Replication

Describe whether the experimental findings were reliably reproduced.

All experiments were reproduced two or more times using the same experimental approach, or in the case of mice or cells, use of two sgRNAs against Keap1 that each contained different targeted sequencing.

4. Randomization

Describe how samples/organisms/participants were allocated into experimental groups.

Mice of the ages between 6-8 weeks of the correct genotypes were randomly selected (no sex-bias) to be included in tumor initiation studies.

Post-mortem tumor burden was quantified in a blinded fashion. The researcher did not know the identity of the mouse or what sgRNA was used (sgTom vs sgKeap1).

5. Blinding

Describe whether the investigators were blinded to group allocation during data collection and/or analysis.

See above. All burden analysis and IHC was done in a blinded fashion, in which the researcher was unaware of which genotype the sample came from. See supplementary materials and methods.

Note: all studies involving animals and/or human research participants must disclose whether blinding and randomization were used.

6. Statistical parameters

For all figures and tables that use statistical methods, confirm that the following items are present in relevant figure legends (or in the Methods section if additional space is needed).

n/a	Confirmed	
☐	☒	The <u>exact sample size</u> (*n*) for each experimental group/condition, given as a discrete number and unit of measurement (animals, litters, cultures, etc.)
☐	☒	A description of how samples were collected, noting whether measurements were taken from distinct samples or whether the same sample was measured repeatedly
☐	☒	A statement indicating how many times each experiment was replicated
☐	☒	The statistical test(s) used and whether they are one- or two-sided (note: only common tests should be described solely by name; more complex techniques should be described in the Methods section)
☐	☒	A description of any assumptions or corrections, such as an adjustment for multiple comparisons
☐	☒	The test results (e.g. *P* values) given as exact values whenever possible and with confidence intervals noted
☐	☒	A clear description of statistics including <u>central tendency</u> (e.g. median, mean) and <u>variation</u> (e.g. standard deviation, interquartile range)
☐	☒	Clearly defined error bars

See the web collection on statistics for biologists for further resources and guidance.

▶ Software

Policy information about availability of computer code

7. Software

Describe the software used to analyze the data in this study.	Prism or R/unix.

For manuscripts utilizing custom algorithms or software that are central to the paper but not yet described in the published literature, software must be made available to editors and reviewers upon request. We strongly encourage code deposition in a community repository (e.g. GitHub). *Nature Methods* guidance for providing algorithms and software for publication provides further information on this topic.

▶ Materials and reagents

Policy information about availability of materials

8. Materials availability

Indicate whether there are restrictions on availability of unique materials or if these materials are only available for distribution by a for-profit company.	All materials are available except: lenti-CRISPR V2 (Addgene) used for the CRISPR Screen pX458 (Addgene) used for generation of the Keap1-mutant cell lines.

9. Antibodies

Describe the antibodies used and how they were validated for use in the system under study (i.e. assay and species).	All antibodies used in this studies are included in the supplementary materials and methods. Antibodies used were previously published or validated using engineered-knock out cell lines.

10. Eukaryotic cell lines

a. State the source of each eukaryotic cell line used.	Murine cell lines used in this study are derived from KP tumor bearing mice. These mice were donated by Leny Gocheva of the Jacks Lab and have been described and published. Human lines were acquired from ATCC.
b. Describe the method of cell line authentication used.	Murine lines are derived by us. Human lines were acquired directly from ATCC.
c. Report whether the cell lines were tested for mycoplasma contamination.	Yes, cell lines have been tested for mycoplasma contamination. Our lab routinely tests for mycoplasma every 6 months.
d. If any of the cell lines used are listed in the database of commonly misidentified cell lines maintained by ICLAC, provide a scientific rationale for their use.	No

▶ Animals and human research participants

Policy information about studies involving animals; when reporting animal research, follow the ARRIVE guidelines

11. Description of research animals

Provide details on animals and/or animal-derived
materials used in the study.

> BL6/SV129 mixed background males and females of 6-8 weeks were used for
> authochthonous development of tumors in the KP model initiated with lentiviral
> PSECC vectors expressing sgTom or sgKeap1.
>
> Nude mice of 6-8 weeks (Jackson labs J:NU) were used for xenograft or orthotopic
> transplantation (females only).
>
> Please see supplementary materials and methods Mice section.

Policy information about studies involving human research participants

12. Description of human research participants

Describe the covariate-relevant population
characteristics of the human research participants.

> No human research participants were used.